The guidance and adhesion protein FLRT2 dimerizes *in cis* via dual Small-X_3-Small transmembrane motifs

Verity Jackson[#,1], Julia Hermann[#,1,6], Christopher J. Tynan[#,2], Daniel J. Rolfe[2], Antreas C. Kalli[3], Anna L. Duncan[1], E. Yvonne Jones[4], Mark S. P. Sansom[1], Marisa L. Martin-Fernandez[,2], Elena Seiradake[*,1], Matthieu Chavent[*,5]*

#These authors contributed equally to this study

1- Department of Biochemistry, University of Oxford, South Parks Road, Oxford, OX1 5RJ, United Kingdom
2- Central Laser Facility, Research Complex at Harwell Science & Technology Facilities Council, Harwell Campus, Didcot, United Kingdom
3- Department of Discovery and Translational Science, Institute of Cardiovascular and Metabolic Medicine, School of Medicine and Astbury Center for Structural Molecular Biology, University of Leeds, United Kingdom
4- Division of Structural Biology, Wellcome Centre for Human Genetics, University of Oxford, Oxford, United Kingdom
5- Institut de Pharmacologie et Biologie Structurale, IPBS, Université de Toulouse, CNRS, UPS, 205 route de Narbonne, 31400, Toulouse, France
6- Present address: German Cancer Research Center (DKFZ), Im Neuenheimer Feld 581, 69120 Heidelberg, Germany

* Correspondence and requests for materials should be addressed to E. S. (email: elena.seiradake@bioch.ox.ac.uk), to M. L. M.F. (email: marisa.martin-fernandez@stfc.ac.uk), or to M. C. (email: matthieu.chavent@ipbs.fr)

Abstract

Fibronectin Leucine-rich Repeat Transmembrane (FLRT 1-3) proteins are a family of broadly expressed single-spanning transmembrane receptors that play key roles in development. Their extracellular domains mediate homotypic cell-cell adhesion and heterotypic protein interactions with other receptors to regulate synapse development and cell guidance. These *in trans* FLRT interactions determine the formation of signaling complexes of varying complexity and function. Whether FLRTs also interact *in cis* remains unknown. Here, we reveal two dimerization motifs in the FLRT2 transmembrane helix. Molecular dynamics simulations and single particle tracking experiments show that these 'Small-X_3-Small' motifs synergize with a third dimerization motif encoded in the extracellular domain to permit the *cis* association and diffusion patterns of FLRT2 on cells. The results point to a competitive switching mechanism between *in cis* and *in trans* interactions which suggests that homotypic FLRT interaction mirrors the functionalities of classic adhesion molecules.

Introduction

Fibronectin Leucine-rich Repeat Transmembrane (FLRT) proteins are a family of cell adhesion molecules (CAMs) that are broadly expressed during vertebrate development[1,2]. FLRTs are unusual CAMs as they perform both cell adhesive and repulsive functions, leading to their definition as Repellent CAMs (ReCAMs)[3,4]. In neurons, FLRTs act as repulsive guidance cues during cortical cell migration[3,5-7], whereby they play key role in cortical folding[8] and as adhesion molecules in synaptic complexes[9,10]. Adhesive FLRT functions are elicited by homotypic binding[1,2] or by binding to the G-protein coupled receptor Latrophilin (Lphn 1-3)[6,9,11,12] on opposing cells while cell repulsion results from interaction with Uncoordinated-5 (Unc5A-D)[4,11]. FLRT also interacts with Unc5 *in cis* to regulate Lphn-mediated adhesion, at least *in vitro*[7]. In migrating neurons, FLRT cooperates with the Lphn-binding receptor Teneurin to form a ternary trans-synaptic complex that mediates cell repulsion[13], while the three proteins also function in promoting synapsing[14]. Thus, FLRT acts in a context-dependent manner to determine the formation of different higher order cell-guidance signalling complexes and regulate brain development[15]. Here we ask whether FLRT forms homotypic *cis* complexes and how this may modulate *cis* and *trans* interactions with other partners.

FLRTs share a common architecture[16] (**Fig. 1A**) beginning with an N-terminal Leucine-Rich Repeat (LRR) extracellular domain, which contains a concave surface on which both FLRT and Lphn bind[3,6]. Unc5 binds to an adjacent surface on the LRR domain, which is compatible at least with Lphn-binding[7]. The LRR domain is linked to a type III fibronectin (FN) domain which then leads into the single-spanning transmembrane (TM) domain and a ~100 amino acid long intracellular domain (ICD) of unknown structure. FLRT2 TM domains contained two consecutives "Small-X_3-Small" motifs[17-19] (**Fig. 1B**) which may promote FLRT interactions *in cis*. Indeed, this motif play fundamental roles in other single-spanning transmembrane receptors, including epidermal growth factor receptor (EGFR), fibroblast growth factor receptor (FGFR), integrins, and EphA receptors[20-26].

Characterizing dynamic membrane protein structures is challenging[18,27,28]. However, the recent developments in molecular dynamics (MD) simulations[29] have provided a powerful tool to study membrane receptors and their interactions[30-35]. Coarse-grained molecular dynamics (CG-MD) simulations have emerged as the method of choice to explore the self-assembly of TMs[36-38] and have been exhaustively validated[39-41]. Combining MD simulations with well-established experimental assays such as Single Molecule Tracking (SMT) microscopy[42,43], which tracks the clustering of receptors[44-49] on live cells, is a powerful approach to provide new insights into the dynamic assemblies of cell receptors[21,33,50].

Here, we use molecular dynamics simulations and live cell SMT experiments to reveal how FLRT2 dimerizes *in cis* via two Small-X_3-Small motifs. Unexpectedly, these motifs work synergistically with the extracellular dimerization motif in the ligand-

binding domain[3] to produce FLRT-FLRT association. The results suggest a bipartite structural mechanism that underlies the diverse functions of FLRT, and a competitive mechanism for *in cis* versus *in trans* binding via the extracellular domain.

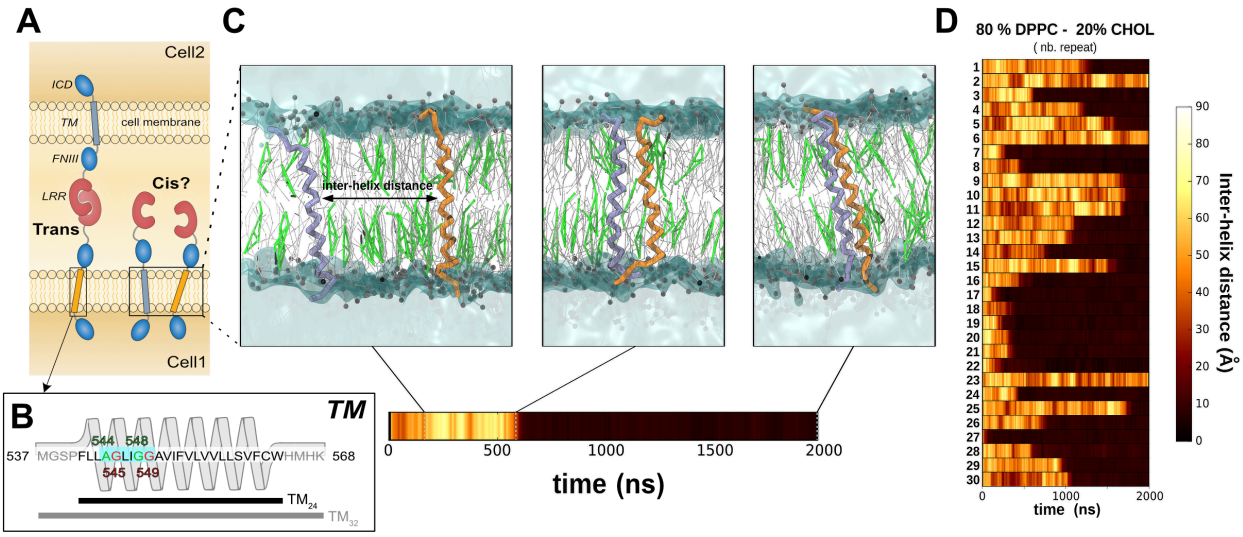

Figure 1: Dimerization of FLRT2 TM domains. A- Schematic of FLRT proteins engaging *in trans* and potentially also *in cis* interactions. **B-**Sequence of the FLRT2 TM helix. The two Small-X_3-Small motifs, key residues for the formation of the helix/helix interface highlighted by the CG-MD simulations, are colored in green and red. Two constructs were used as inputs for MD simulations: the core TM helix of 24 residues (TM_{24}) and an extended version with the four most N- and C-terminal residues (TM_{32}). **C-** The CG-MD protocol to assess TM helix interactions. The two helices are positioned 60 Å apart and diffuse freely in the membrane. The colored bars show, for each simulation, the distance in between the two TM helices as a function of the time. **D-** The TM contact bars of the 30 simulations for the TM_{32} helices in a membrane of 80% POPC and 20% cholesterol. Details for all the simulations can be found in Sup. Fig. 1 and Sup. Fig. 2.

Results

FLRT2 TM dimerization involves two Small-X_3-Small motifs

As no structural information exists for the FLRT2 TM domain, we have used secondary structure prediction tools (see Methods) to predict the membrane-embedded helical region of FLRT2 (**Fig. 1B**). We obtained 24 residues as the core TM helix (denoted TM_{24}). This length is consistent with the average length for a plasma membrane-spanning TM helix[51]. We also extended the helical segment with four N- and C-terminal residues, which were modelled as coils (denoted TM_{32}).

We then performed multiple runs of coarse-grained molecular dynamics (CG-MD) to model the associations of both TM_{24} and TM_{32} in three different types of membrane: POPC, DPPC, and a lipid mixture of 80% POPC and 20% cholesterol (**Sup. Table 1**). For each of these three lipid compositions, we positioned the two helices 60 Å apart allowing them to diffuse freely until there is an encounter which predominantly leads to the formation of a stable helix dimer (**Fig. 1D and Sup. Fig. 1**

101 **and 2**). The TM helices interacted through a network of residues distributed along each
102 peptide. Among these residues, we identified two consecutive Small-X_3-Small motifs
103 known to favor TM interactions[52,53]: A_{544}-X3- G_{548} and G_{545}-X3-G_{549} (**Sup. Fig. 3**).

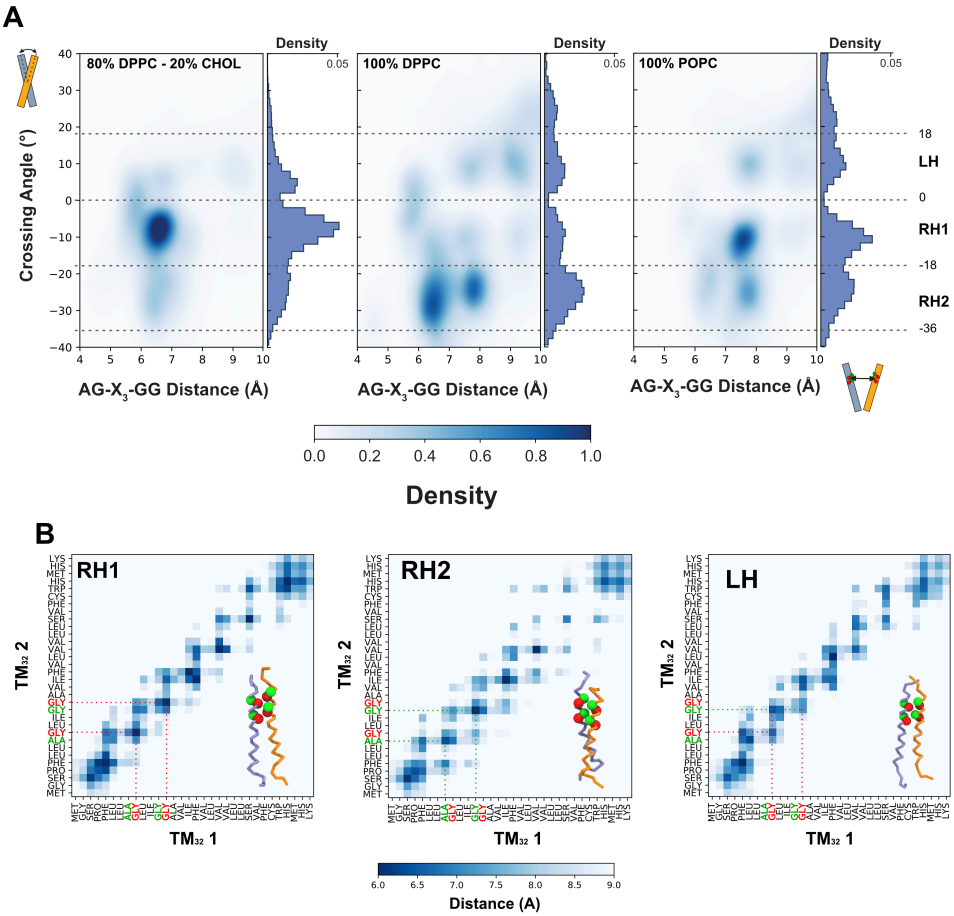

Figure 2: CG-MD simulations uncover two Small-X_3-Small motifs as key areas for the dimerization of FLRT2 TM domains. A- TM_{32} helix dimer structural populations for different membrane compositions (see Sup. Fig. 5 to 7 for individual simulations). A positive value for the crossing angle corresponds to a left-handed (LH) dimer, and a negative value to a right-handed (RH) dimer (details for TM_{24} systems are presented in Sup. Fig. 4 and Sup. Fig. 8 to 10). The simulations have highlighted two Right Handed conformations (RH1 and RH2) and one Left Handed (LH). RH1 is defined with a crossing angle between -18° and 0°, RH2 between -36° and -18°, and LH between 0° and 18°. **B-** The three main representative structures for each crossing angle peak with A_{544}-G_{548} dimerization motif in green, and A_{545}-G_{549} dimerization motif in red. For each conformation (RH1, RH2 and LH), averaged TM contact matrix extracted from simulations of TM_{32} in 80% DPPC and 20% of cholesterol highlight the TM dimerization via the A_{544}-G_{548} motif (RH2), G_{545}-G_{549} motif (RH1) or a combination of both (LH).

104

105 We next performed crossing angle analysis to analyze the geometry of the TM
106 helices[54,55]. For both the TM_{24} and TM_{32} models, this revealed three dimer populations
107 (**Fig. 2A and Sup. Fig. 4**): two main right-handed populations with average crossing
108 angles of approximately -27° (RH1) and -9° (RH2) and one minor left-handed
109 population with an average crossing angle of around +9° (LH). For each crossing angle
110 population, a clear interface was identified (**Fig. 2B**). RH1 conformations were driven

111 by interactions around the G_{545}-X_3-G_{549} motif while RH2 conformations were centered
112 on the A_{544}-X_3-G_{548} motif. The LH population was constituted by peptides interacting
113 via both motifs.
114 To obtain a more detailed view of the dynamical TM dimer association, we
115 plotted the helix crossing angle against the distance between the two Small-X_3-Small
116 motifs. This revealed several sub-populations associated with each crossing angle
117 peak (**Fig. 2A**). Notably, membrane lipid composition appeared to modulate this
118 dynamical equilibrium (**Fig. 2A and Sup. Fig. 4**) as seen in other studies[56-60].
119 Furthermore, for each membrane composition, the juxtamembrane regions appeared
120 to modulate TM dimer formation (**Fig. 2A and Sup. Fig. 4**) as previously reported[61].
121 Plotting individual simulations (**Sup. Fig. 5 to 10**) suggested that the RH1
122 conformation can exchange with the LH conformation. RH2 seemed to also exchange
123 with RH1 conformation but to a lesser extent. Thus, RH1 may be seen as a transition
124 state in between RH1 and LH conformations.
125 We then refined the three main TM dimer structures (RH1, RH2 and LH) by
126 performing 400 ns of atomistic MD simulations (see Methods) (**Sup. Fig. 11-A**). The
127 RH1 and RH2 dimers remained in a right-handed conformation though we observed a
128 slight increase of the crossing angle for the RH2 structure (with a final crossing angle
129 of -37°). Interestingly, the LH structure switched to a right-handed conformation at the
130 beginning of the simulation and then returned to a stable left-handed conformation.
131 This confirmed the exchanges between RH1 and LH configurations seen in coarse-
132 grain simulations (**Sup. Fig. 5 to 10**). For all three structures, the interactions between
133 the Small-X3-Small motifs were stable throughout the simulation (**Sup. Fig. 11-B**).
134 Thus, MD simulations revealed a dynamic equilibrium of dimer structures
135 involving the two consecutives Small-X_3-Small motifs: A_{544}-X3- G_{548} and G_{545}-X3-G_{549}.
136
137 **Distinctive mutations in the Small-X_3-Small motifs selectively modulate FLRT2**
138 **TM dimerization**
139 To assess the individual contributions of the two Small-X_3-Small motifs to the
140 dimerization, we performed CG-MD simulations with several mutants replacing glycine
141 residues with isoleucine or valine residues, the larger hydrophobic side chains of which
142 are expected to disturb the TM dimerization[62-66] (**Fig. 3A and Sup. Table 1**). For each
143 mutant, we evaluated both the crossing angle populations and the spatial distributions
144 for the TM_{32} construct in a DPPC bilayer.

A

Protein	Mutation	Mutation Position
FLRT2	WT	-
	LRR	R186N+D188T
	TM_0	A544I
	TM_1	A544I-G548I
	TM_2	G545I-G549I
	TM_3	G545V
	TM_{1+2}	A544I/G545I-G548I/G549I
	LRR/TM_{1+2}	R186N+D188T + A544I/G545I-G548I/G549I

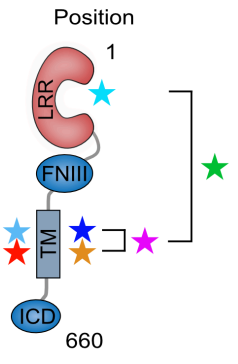

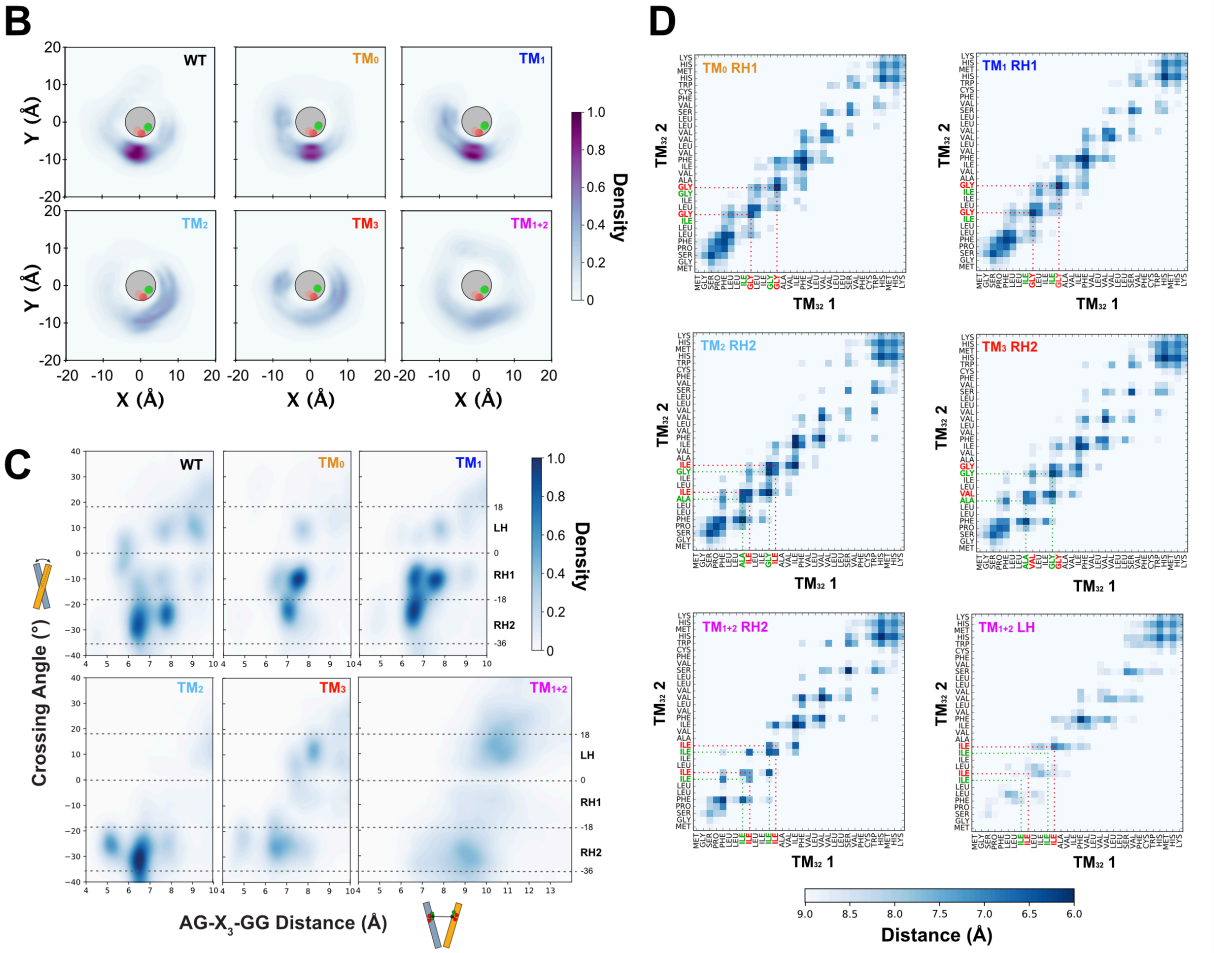

Figure 3: *In silico* mutations in the two Small-X_3-Small motifs affect the TM dimerization and dynamical equilibrium. A- Table of mutations for *in silico* and SMT experiments. The LRR/TM_{1+2} mutant was only used for the SMT experiments. **B-** Spatial distribution profiles of one TM_{32} helix relative to the other for the CG simulations of both WT and mutants. The diagram shows the probability density of finding the backbone particles of one TM_{32} helix at a given point in the bilayer plane around the other helix. Diagrams are colored such that white represents low probability up to blue for higher probabilities. Green (respectively red) circles depict averaged positions of A_{544} and G_{548} (respectively G_{545} and G_{549}) residues. **C-** Helix crossing angle distributions for both TM_{32} WT and mutants. **D-** Averaged TM contact matrices of the different mutants based on different representative TM conformations.

146 In contrast with the wild type, mutations in the A_{544}-X_3-G_{548} motif (mutants TM_0
147 and TM_1) favored formation of a dimer with a spatial distribution focused on the G_{545}-
148 X_3-G_{549} motif (**Fig. 3B**) and switched of crossing angle populations towards RH1
149 conformations (**Fig. 3C**). For these conformations, TM helices are packed around the
150 G_{545}-X_3-G_{549} motif (**Fig. 3D**). Mutations in the G_{545}-X_3-G_{549} motif (mutants TM_2 and TM_3)
151 drove interactions through the G_{544}-X_3-G_{548} motif (**Fig. 3B,D**) favoring RH2 crossing
152 angle populations (**Fig. 3C**) and allowing TM domains to explore a wider area around
153 the G_{544}-X_3-G_{548} motif compared to the WT (**Fig. 3B**). Mutations of both motifs (mutant
154 TM_{1+2}) enabled one TM domain to explore the entire bilayer plane surrounding its TM
155 partner (**Fig. 3B**), thereby abolishing the specificity of the TM helix interactions. For
156 this double mutant, the crossing angle density was clearly more diffuse than for the
157 WT or the other mutants, further highlighting a loss of specificity (**Fig. 3C**). Mutating
158 both motifs also limited the interactions in between the TM helices for the two main
159 conformations RH2 and LH (**Fig. 3D**).
160 Thus, these mutations highlighted two distinct dynamical behaviors of the TMD
161 dimer specific to each motif. Only mutation of both motifs resulted in an almost
162 complete loss of interactions between the two monomers.
163
164 **Mutations in the Small-X_3-Small motifs affect FLRT2 co-localization in cells**
165 To support the *in silico* results, we performed SMT experiments to assess the
166 contribution of the predicted key residues in the Small-X_3-Small motifs to dimer
167 formation by mutating glycine residues to isoleucine or valine residues (**Fig. 3A**). We
168 tracked FLRT2 receptors on live cells with a sub-pixel accuracy by SMT in two different
169 channels using the dyes Alexa549 and CF640R (**Fig. 4A-C**). Based on receptor frame
170 to frame proximity in each channel (**Fig. 4C**), we then built a distribution of the durations
171 of co-localization events (**Fig. 4D**), referred to as τ_{on}. The duration of co-localization
172 events is a characteristic of the stability of any interaction or association between the
173 tracked receptors, and is independent of expressed receptor concentration[47].
174 Comparing the τ_{on} distributions of WT and mutants (**Fig. 4E**) revealed that mutations
175 in only one of the two motifs (either TM_1, TM_2 or TM_3 alone) was insufficient to reduce
176 the baseline average τ_{on} of wild-type FLRT2. However, mutation of both Small-X_3-
177 Small motifs (TM_{1+2} mutant) resulted in a significant shift in the τ_{on} distribution towards
178 lower values (**Fig. 4E and Sup. Fig. 12B**). These results are in agreement with a
179 previous study showing that mutation of both Small-X_3-Small transmembrane motifs is
180 necessary to disrupt the EGFR TM dimer and affect receptor function[67]. The significant
181 shift in τ_{on} was also seen for the mutation in the LRR ectodomain, known to abolish
182 FLRT-FLRT trans-interactions[3], and for the triple mutation LRR+TM_{1+2}. This provides
183 experimental support for the *in silico* results demonstrating that the two Small-X_3-Small
184 motifs are required for FLRT interactions *in cis*.
185

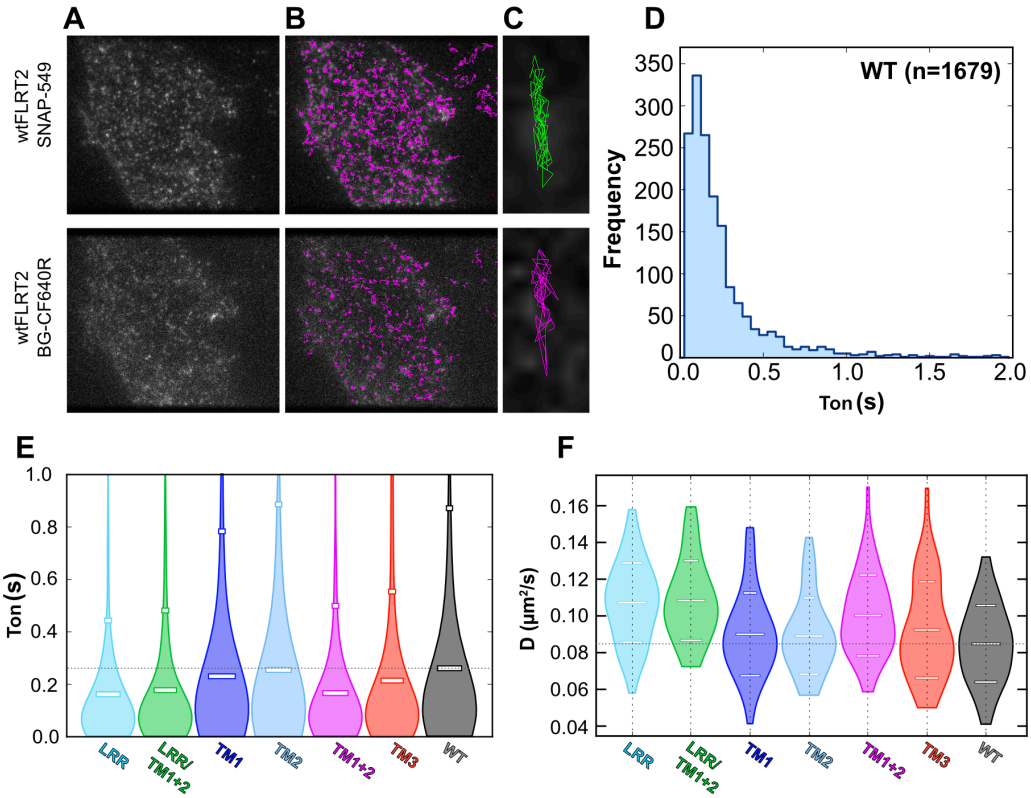

Figure 4: Mutations in the TM domains affect colocalization of FLRT2 monomers at the cell surface. A- Single molecule TIRF image of HeLa cells expressing wtFLRT2 labelled with both SNAP-549 and BG-CF640R. **B-** Single molecule tracks are generated from time series of the molecules under observation. **C-** An example pair of colocalized tracks where the tracks are separated by less than 1 pixel (160 nm) during at least 5 frames (250 ms). **D-** Example τ_{on} distribution for the WT (n represents the number of tracks analyzed). **E-** Distributions of τ_{on} for wtFLRT2 and each of the six FLRT2 mutants tested. Significance analysis of these distributions available in Sup. Fig 12B. **F-** Distributions of diffusion values for wtFLRT2 and each of the six FLRT2 mutants tested. Significance analysis of these distributions available in Sup. Fig 12C.

We next analyzed the diffusion coefficients for the WT and mutants as an alternative approach to provide further insight into the role of these motifs in dimer formation (**Fig. 4F**). In line with the τ_{on} results, only diffusion values for the mutants TM_{1+2}, LRR, and LRR+TM_{1+2}, increased significantly from the WT (**Sup. Fig. 12C,D**). Notably, diffusion calculations in MD simulations also indicated a significant difference in between the double mutant TM_{1+2} and the WT (**Sup. Fig. 12E**). Although the spatial resolution of single molecule tracking is insufficient to discriminate between direct pairwise interactions and co-confinement or joint interactions with the same larger protein complex, this correlation between the decreased duration of co-localization events and the increased diffusion constant of the tracked receptors is consistent with the mutations disrupting interactions that usually occur between WT FLRT2 TM domains.

Taken together, these data indicate that the extracellular motif and both G_{544}-X_3-G_{548} and G_{545}-X_3-G_{549} motifs in the transmembrane region are required for wild-type FLRT2 homotypic interactions *in cis*.

Discussion

TM dimer association is a highly dynamic process involving multiple states and weak interactions hence challenging structural studies. As a consequence, only a limited number of TM dimer structures are available and these are often restricted to one state of the TM dimer[68]. To complement structural studies, MD simulations can provide details of these dynamic assemblies. Here, we have used MD simulations to gain structural insights into the formation of FLRT2 TM dimers. Our models revealed a dynamical equilibrium between conformations involving two successive Small-X_3-Small motifs: G_{544}-X_3-G_{548} and G_{545}-X_3-G_{549} motifs. To further assess these models and the conformational changes governing the FLRT2 dimer association, one could use

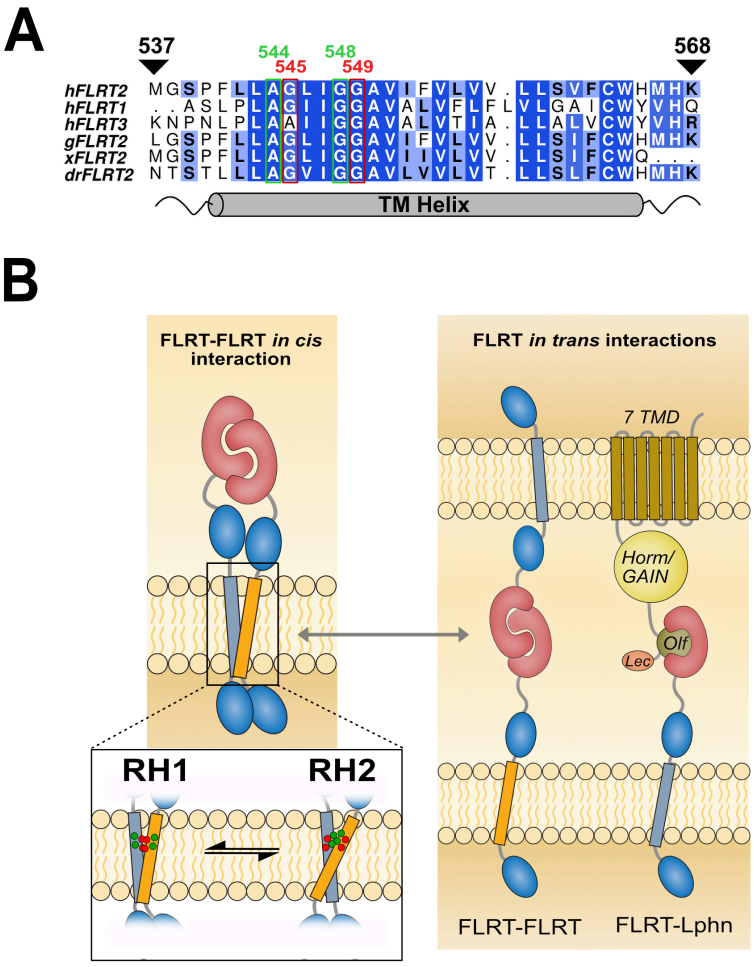

Figure 5: Model of the FLRT *cis*-interaction. A- Sequence alignment of the TM domain for FLRT1-3 in human and for FLRT2 in other species (human:h, chicken:g, frog:x, fish:dr). **B-** Model of FLRT2 cis-interactions that may compete with different FLRT2 trans interactions. The interconversion in between RH1, involving the G_{545}-G_{549} motif (in red), and RH2 interactions, driven by the A_{544}-G_{548} motif (in green), may be modulated by mutations in the TM domain or environmental conditions such as changes in the lipid composition of the membrane.

accelerated MD simulations combined with free energy calculations[69,70]. To enable this, we are releasing the three main conformations (RH1, RH2 and LH) both in coarse

grained and atomistic representations (https://github.com/MChavent/FLRT).

The TM helices of other receptors such as EGFRs and EPHAs dimerize via Small-X_3-Small motifs to transduce extracellular signals into intracellular activity[21,22,24]. Unlike these receptors, there is no enzymatic activity associated with FLRT. Instead, FLRTs act as crucial adaptor proteins that define the architecture of cell surface signalling hubs[3,7,13], and also regulate the trafficking of diverse receptors. For example, FGF receptor traffics with FLRT1-3[71,72], while FLRT3 regulates the cell surface levels of the Deleted in Colorectal Carcinoma (DCC) receptor in thalamic axons[73]. Dimerization of the EGFR Small-X_3-Small motif also regulates EGFR trafficking[65]. Thus, *in cis* dimerization via the Small-X_3-Small motifs in the TM helix of FLRTs may act similarly and play a central role in receptors trafficking and thereby signal transduction.

A functional role for the Small-X_3-Small motifs is supported by their conservation in all three FLRT human homologues (FLRT 1-3) as well as for FLRT2 in different species (**Fig. 5A**). In addition, the COSMIC database[74] lists a number of cancer-related mutations targeting the TM domain of FLRT2. Two such mutations (A544V and G545V) map to the Small-X_3-Small motifs described here, and may affect FLRT2 function and dynamics as seen in MD simulations (**Fig. 3**). Furthermore, the lipid environment can modulate WT TM association[75-77] (**Fig. 2A, Sup. Fig. 4**) and may accentuate deleterious effects of these mutations.

Unexpectedly, our results show that the same mutation in the LRR domain that disrupts FLRT-FLRT interactions *in trans*[3] also disrupts FLRT-FLRT interaction *in cis*, posing the question whether FLRT *cis* and *trans* interactions are competitive (**Fig. 5B**). Adding complexity to this issue is the observation that the same mutation also abolishes *trans* FLRT-Lphn interactions[3,6]. These findings suggest that Lphn may also compete with *in cis* FLRT-FLRT dimerization, leading to a mechanism in which FLRTs switch between *in cis* dimerization and *in trans* interactions (**Fig. 5B**). Interplay between *cis* and *trans* interactions are essential for the formation of clusters of adhesion proteins leading to cell-cell recognition[78]. One canonical example is the formation of adherens junction by the clustering of cadherins for which both *cis* and *trans* interactions are required[79,80]. In addition, a competitive switch between *in trans* and *in cis* interactions occurs for EphA receptors with their ephrin-A ligands[81,82]. Our results describe the structural basis and nature of *in cis* dimerization of FLRT2 receptors and suggest how these interactions may compete with interactions *in trans* to determines the formation of specific signalling complexes and regulate fundamental developmental processes, such as cortical folding and synapsing.

Acknowledgements

A.L.D. is supported by the BBSRC grant BB/R00126X/1 and Pembroke College, Oxford (BTP Fellowship). E.Y.J. was funded by UK Medical Research Council programme grant G9900061. The Wellcome Centre for Human Genetics is supported

by Wellcome Trust Centre grant 203141/Z/16/Z. E.S. is funded by the Wellcome Trust (202827/Z/16/Z), EMBO YIP and supported by the COST action 'Adhere'n Rise'. V.A.J was funded by the Wellcome Trust DPhil programme in Cellullar Structural Biology. M.S.P.S. is funded by Wellcome Trust grants WT092970MA and 208361/Z/17/Z. M. C. is supported by the CNRS-MITI grant “Modélisation du vivant” 2020. This work was granted access to the HPC resources of CALMIP supercomputing center under the allocation 2020-17036. The single molecule analysis used computing resources provided by STFC Scientific Computing Department's SCARF cluster. We acknowledge Life Science Editors for proofreading the manuscript. M. C. thanks E. Haanappel and A. Atkinson for fruitful discussions and support.

Competing interests

No competing interests declared

Methods

Modeling Transmembrane domain and Molecular Dynamics Simulations

Results from the PSIpred[83], PRED-TMR2[84], and HMMTOP[85] servers were combined to predict the membrane embedded helical region of FLRT2. Twenty-four residues of human FLRT2 (residues 541 – 564) were selected to form the core of the TM helix (TM_{24}). The transmembrane domain was created using the Pymol secondary structure creation script: build_seq.py (http://pldserver1.biochem.queensu.ca/~rlc/work/pymol/) and then converted into coarse-grained model. For TM_{32}, the four residues both N- and C-terminal of TM24 were modelled as random coils using Modeller 9v9[86].

Coarse-grained MD (CG-MD) simulations were performed using GROMACS 4.6 (www.gromacs.org)[87,88] with the MARTINI 2.1 forcefield[89,90]. The temperature was 323K. Electrostatic interactions were shifted to zero between 0 and 1.2 nm and the Lenard-Jones interactions between 0.9 and 1.2 nm. A Berendsen thermostat in combination with a Berendsen barostat[91] with a coupling constant of 1.0 ps, a compressibility of 5.0 x 10^{-6} bar^{-1}, and a reference pressure of 1 bar were used. The integration timestep was 20 fs. Simulations were run for either 1 or 2 μs (**Sup. Table 1**) over twenty to thirty replicates to ensure exhaustive sampling of TM helix dimer structures.

We then converted the three main representative (RH1, RH2, and LH) coarse grained structures into atomistic models using the CHARMM-GUI MARTINI to All-atom converter (http://www.charmm-gui.org/?doc=input/converter.martini2all). Atomistic simulations were performed with GROMACS 2018 in combination with the CHARMM36 forcefield[92-94] and TIP3P water model. The temperature was held at 310K. A first step of energy minimization was performed using the steepest descent algorithm and was equilibrated with a constant temperature (canonical ensemble, NVT, 310 K) ensemble for 100 picoseconds, followed by a 100 picoseconds equilibration at constant pressure (isothermal-isobaric, NPT, 1 bar). We then ran 100 ns of equilibration by keeping the protein backbone constrained followed by 400 ns of unrestrained production run. We applied a Nosé-Hoover thermostat on the system, coupled with the Parrinello–Rahman barostat, with a compressibility of 4.5x10^{-5} bar^{-1}. Long-range electrostatics were modeled using the Particle-Mesh Ewald method[95]. All bonds were treated using the LINCS algorithm[96]. The integration time step was 1 femtosecond.

Simulation analysis:

Protein and lipid structures were rendered using VMD[97]. Simulations trajectories were analyzed using a combination of Tcl/VMD and Python scripts. Matplotlib was used to create graphs and images of TMD monomer distances, contact matrices, TMD density rendering, and crossing angles analysis. All the scripts used to

311 perform these analyses are available at: https://github.com/MChavent/FLRT.
312 Distances were calculated in between the two centers of mass of each TM helix.
313 Density, TM contacts and crossing angles calculations were performed every
314 nanosecond for the part of the trajectory where a dimer was formed. In Figure 2-A
315 (resp. 3-B,C), the values were renormalized to take into account of both the maximum
316 values and time of interactions to properly compare the different membrane (resp. Wild
317 Type and mutants) systems.
318 Diffusion analyses of dimers were carried out by extracting time-averaged
319 mean squared displacement (MSD) for all simulation replicates, for the part of the
320 trajectory where a dimer was formed. For each replicate, a MSD vs. Δt was plotted for
321 Δt in the range 0.2 ns – 200 ns. The diffusion coefficient (D) for each trajectory was
322 calculated by fitting the equation $MSD = 4D\Delta t$ to the first two points in the plot, in order
323 to obtain an instantaneous diffusion coefficient. The diffusion analysis script used to
324 perform the analysis can be found at:
325 https://github.com/tylerjereddy/diffusion_analysis_MD_simulations.
326
327 **Cloning**
328 SNAP-FLRT2 was cloned into the EcoRI/XhoI restrictrion sites of the pHSec
329 vector[98]. In SNAP-FLRT2 an N-terminal SNAP tag (containing the RPTPσ signal
330 sequence) was fused to murine FLRT2 (residues A35 – T660) via an HA-tag. Mutations
331 were introduced using molecular cloning.
332
333 **Cell Culture and Transfection**
334 HeLa cells were seeded onto uncoated 4-well µ-Slides, #1.5 polymer coverslips
335 (Ibidi) at a density of 1.1x105 cells/well in 600 µL phenol red-free DMEM + 10% FBS
336 + 1% L-Gln + 1% NEAA (complete medium). After 24 h, each well was transfected with
337 2.0 µg plasmid DNA using FuGENE6, according to the manufacturer's instructions.
338 Cells were maintained at 37 °C, 5% CO2 and were prepared for experiments 12-18
339 hours post-transfection.
340
341 **BG-CF640R Conjugation**
342 CF640R succinimidyl ester (Biotium) was reacted with BG-NH2 (New England
343 Biolabs) to produce the benzylguanine functionalised dye BG-CF640R. 1 µmol of
344 CF640R succinimidyle ester was reconstituted in DMSO and dissolved in 10 ml 0.1 M
345 sodium bicarbonate buffer at pH 8.4. 1.5 µmol BG-NH2 in DMSO was added to the
346 dye mixture and vortexed well. The reaction was shaken at room temperature
347 overnight before dilution with deionised water. For all subsequent dilutions the
348 conjugation efficiency was assumed to be 100%.
349
350

351 **Two-Colour Fluorescent Labelling**

352 To achieve an approximately equal ratio of single molecules labelled with
353 SNAP Dy549 and BG-CF640R a two-step staining procedure was used. Firstly, the
354 medium was removed from each well of the 4-well μ-Slides and the cells washed twice
355 with 300 μL complete medium. BG-CF60R was diluted in complete medium to a final
356 concentration of 10 nM and applied to each well of the μ-Slide for 5 min. The medium
357 was then exchanged for 150 μL 10 nM SNAP-Dy549 (SNAP-Surface 549, New
358 England Biolabs) in complete medium and incubated for a further 5 min. All labelling
359 steps were performed at 37 oC, 5% CO2. Labelled cells were then washed three times
360 with complete medium and the final wash replaced with Live Cell Imaging Solution plus
361 1:50 ProLong Antifade reagent (both ThermoFisher) and incubated for at least 15 min,
362 at 37 ^{o}C, 5% CO2 before beginning experiments.
363

364 **Single molecule image acquisition and feature tracking**

365 Single-molecule images were acquired using an Axiovert 200M microscope
366 with an iLas2 TIRF illuminator (Cairn, UK), with a ×100 oil-immersion objective (α-Plan-
367 Fluar, NA = 1.46; Zeiss, UK) and an EMCCD (iXon X3; Andor, UK). The microscope is
368 also equipped with a wrap-around incubator (Pecon XL S1). The 561 and 642 nm lines
369 of a LightHub laser combiner (Omicron-laserage Laserprodukte GmbH) were used to
370 illuminate the sample and an Optosplit Image Splitter (Cairn Research) was used to
371 separate the image into its spectral components as described previously[99]. The field
372 of view of each channel for single-molecule imaging was 80 × 30 μm. Typically, for
373 each condition at least 50 fields of view comprising one or more cells were acquired
374 from a total of 4 independent biological replicates. Single molecules were tracked in
375 each field of view for 30s, by which time the majority of molecules had undergone
376 photobleaching. All single-molecule time series data were analyzed using the
377 multidimensional analysis software described previously[100]. Briefly, this software
378 performs frame-by-frame Bayesian segmentation to detect and measure features to
379 sub-pixel precision, then links these features through time to create tracks using a
380 simple proximity-based algorithm. The software determines cubic polynomial
381 registration transformations between wavelength channels from images of fluorescent
382 beads. Feature detection and tracking was performed independently in each channel.
383

384 **Calculation of colocalisation and τ_{ON}**

385 Two-colour TIRF images of the basolateral surfaces of cells were chromatically
386 separated by a beam splitter and registered using custom-made software to map the
387 relative positions of the probes over the time course of data acquisition[100] and extract
388 single molecule tracks. A colocalisation event was defined as one in which a track in
389 one channel moves within one pixel of a track in the other channel before they move
390 apart again (**Sup. Fig 12A**). The duration of each such event is one measurement of
391 τ_{ON}. This parameter indicates the stability of presumptive receptor interactions while

392 beingin sensitive to variation in expression of the receptors between cells or different
393 levels of labelling with the two probes within cells[47]. The track positions were registered
394 between channels prior to this analysis. To reduce the impact of localisation error on
395 these results a temporal Gaussian smoothing filter of FWHM 4 frames (200 ms) was
396 applied to the position traces before the colocalisation analyses. τ_{ON} distributions were
397 compared between conditions using the two sample Kolmogorov-Smirnov test to
398 decide which were significantly different (**Sup. Fig 12B**).
399
400 **Mean squared displacement and diffusion calculation**
401 From single particle tracks, mean squared displacement (MSD) curves were calculated
402 as $MSD(\Delta T)=\langle|\mathbf{r}_i(T+\Delta T)-\mathbf{r}_i(T)|^2\rangle$ where $|\mathbf{r}_i(T+\Delta T)-\mathbf{r}_i(T)|$ is the displacement between
403 position of track *i* at time *T* and time $T+\Delta T$ and the average is over all pairs of points
404 separated by ΔT in each track. The average instantaneous diffusion coefficient (D) for
405 these tracks was calculated by fitting a straight line to the first two points of the MSD
406 curve then calculating D directly from the gradient m of the fit, D=m/4. The tracks for
407 each single molecule field of view (FOV) were pooled into one MSD curve per FOV to
408 produce a sample of D values, one value per FOV per condition. These D distributions
409 were compared between conditions using the Kolmogorov-Smirnov test to decide
410 which were significantly different.

References

1. Karaulanov, E. E., Böttcher, R. T. & Niehrs, C. A role for fibronectin-leucine-rich transmembrane cell-surface proteins in homotypic cell adhesion. *EMBO Rep* **7,** 283–290 (2006).
2. Maretto, S. *et al.* Ventral closure, headfold fusion and definitive endoderm migration defects in mouse embryos lacking the fibronectin leucine-rich transmembrane protein FLRT3. *Dev. Biol.* **318,** 184–193 (2008).
3. Seiradake, E. *et al.* FLRT structure: balancing repulsion and cell adhesion in cortical and vascular development. *Neuron* **84,** 370–385 (2014).
4. Yamagishi, S. *et al.* FLRT2 and FLRT3 act as repulsive guidance cues for Unc5-positive neurons. *EMBO J.* **30,** 2920–2933 (2011).
5. S, Y. *et al.* FLRT2 and FLRT3 act as repulsive guidance cues for Unc5-positive neurons. *EMBO J.* **30,** 2920–2933 (2011).
6. Jackson, V. A. *et al.* Structural basis of latrophilin-FLRT interaction. *Structure (London, England : 1993)* **23,** 774–781 (2015).
7. Jackson, V. A. *et al.* Super-complexes of adhesion GPCRs and neural guidance receptors. *Nat Commun* **7,** 11184 (2016).
8. del Toro, D. *et al.* Regulation of Cerebral Cortex Folding by Controlling Neuronal Migration via FLRT Adhesion Molecules. *Cell* **169,** 621–635.e16 (2017).
9. O'Sullivan, M. L. *et al.* FLRT proteins are endogenous latrophilin ligands and regulate excitatory synapse development. *Neuron* **73,** 903–910 (2012).
10. Sando, R., Jiang, X. & Südhof, T. C. Latrophilin GPCRs direct synapse specificity by coincident binding of FLRTs and teneurins. *Science* **363,** eaav7969 (2019).
11. Lu, Y. C. *et al.* Structural Basis of Latrophilin-FLRT-UNC5 Interaction in Cell Adhesion. *Structure (London, England : 1993)* **23,** 1678–1691 (2015).
12. Ranaivoson, F. M. *et al.* Structural and Mechanistic Insights into the Latrophilin3-FLRT3 Complex that Mediates Glutamatergic Synapse Development. *Structure (London, England : 1993)* **23,** 1665–1677 (2015).
13. del Toro, D. *et al.* Structural Basis of Teneurin-Latrophilin Interaction in Repulsive Guidance of Migrating Neurons. *Cell* **180,** 323–339.e19 (2020).
14. Sando, R., Jiang, X. & Südhof, T. C. Latrophilin GPCRs direct synapse specificity by coincident binding of FLRTs and teneurins. *Science* **363,** eaav7969 (2019).
15. Seiradake, E., Jones, E. Y. & Klein, R. Structural Perspectives on Axon Guidance. *Annu. Rev. Cell Dev. Biol.* **32,** 577–608 (2016).
16. Lacy, S. E., Bönnemann, C. G., Buzney, E. A. & Kunkel, L. M. Identification of FLRT1, FLRT2, and FLRT3: a novel family of transmembrane leucine-rich repeat proteins. *Genomics* **62,** 417–426 (1999).
17. Anderson, S. M., Mueller, B. K., Lange, E. J. & Senes, A. Combination of Cα-H Hydrogen Bonds and van der Waals Packing Modulates the Stability of GxxxG-Mediated Dimers in Membranes. *J. Am. Chem. Soc.* **139,** 15774–15783 (2017).
18. Bugge, K., Lindorff-Larsen, K. & Kragelund, B. B. Understanding single-pass transmembrane receptor signaling from a structural viewpoint-what are we missing? *FEBS J.* **283,** 4424–4451 (2016).
19. Cymer, F., Veerappan, A. & Schneider, D. Transmembrane helix-helix interactions are modulated by the sequence context and by lipid bilayer properties. *Biochim. Biophys. Acta* **1818,** 963–973 (2012).
20. Bocharov, E. V. *et al.* Structure of FGFR3 Transmembrane Domain Dimer: Implications for Signaling and Human Pathologies. *Structure (London, England : 1993)* **21,** 2087–2093 (2013).
21. Brooks, A. J. *et al.* Mechanism of Activation of Protein Kinase JAK2 by the Growth Hormone Receptor. *Science* **344,** 1249783–1249783 (2014).
22. Fleishman, S. J., Schlessinger, J. & Ben-Tal, N. A putative molecular-activation switch in the transmembrane domain of erbB2. *Proc. Natl. Acad. Sci. U.S.A.* **99,** 15937–15940 (2002).
23. Lau, T.-L., Kim, C., Ginsberg, M. H. & Ulmer, T. S. The structure of the integrin alphaIIbbeta3 transmembrane complex explains integrin transmembrane signalling. *EMBO J.* **28,** 1351–1361 (2009).
24. Bocharov, E. V. *et al.* Left-handed dimer of EphA2 transmembrane domain: Helix packing diversity among receptor tyrosine kinases. *Biophys. J.* **98,** 881–889 (2010).
25. Artemenko, E. O., Egorova, N. S., Arseniev, A. S. & Feofanov, A. V. Transmembrane domain of EphA1 receptor forms dimers in membrane-like environment. *Biochim. Biophys. Acta* **1778,** 2361–2367 (2008).
26. Bocharov, E. V. *et al.* Structural basis of the signal transduction via transmembrane domain of the human growth hormone receptor. *Biochimica et Biophysica Acta (BBA) - General Subjects* **1862,** 1410–1420 (2018).
27. Zhang, Q. & Cherezov, V. Chemical tools for membrane protein structural biology. *Curr. Opin. Struct. Biol.* **58,** 278–285 (2019).
28. Cross, T. A., Sharma, M., Yi, M. & Zhou, H.-X. Influence of solubilizing environments on membrane protein structures. *Trends Biochem. Sci.* **36,** 117–125 (2011).
29. Bottaro, S. & Lindorff-Larsen, K. Biophysical experiments and biomolecular simulations: A

perfect match? *Science* **361,** 355–360 (2018).
30. Mravic, M. *et al.* Packing of apolar side chains enables accurate design of highly stable membrane proteins. *Science* **363,** 1418–1423 (2019).
31. Kalli, A. C., Campbell, I. D. & Sansom, M. S. P. Multiscale simulations suggest a mechanism for integrin inside-out activation. *Proc Natl Acad Sci USA* **108,** 11890–11895 (2011).
32. Arkhipov, A. *et al.* Architecture and membrane interactions of the EGF receptor. *Cell* **152,** 557–569 (2013).
33. Wilmes, S. *et al.* Mechanism of homodimeric cytokine receptor activation and dysregulation by oncogenic mutations. *Science* **367,** 643–652 (2020).
34. Chavent, M. *et al.* Interactions of the EphA2 Kinase Domain with PIPs in Membranes: Implications for Receptor Function. *Structure (London, England : 1993)* **26,** 1025–1034.e2 (2018).
35. Kaszuba, K. *et al.* N-Glycosylation as determinant of epidermal growth factor receptor conformation in membranes. *Proc Natl Acad Sci USA* **112,** 4334–4339 (2015).
36. Chavent, M., Chetwynd, A. P., Stansfeld, P. J. & Sansom, M. S. P. Dimerization of the EphA1 Receptor Tyrosine Kinase Transmembrane Domain: Insights into the Mechanism of Receptor Activation. *Biochemistry* **53,** 6641–6652 (2014).
37. Wassenaar, T. A. *et al.* High-Throughput Simulations of Dimer and Trimer Assembly of Membrane Proteins. The DAFT Approach. *J. Chem. Theory Comput.* **11,** 2278–2291 (2015).
38. Hall, B. A., Halim, K. B. A., Buyan, A., Emmanouil, B. & Sansom, M. S. P. Sidekick for Membrane Simulations: Automated Ensemble Molecular Dynamics Simulations of Transmembrane Helices. *J. Chem. Theory Comput.* **10,** 2165–2175 (2014).
39. Kalli, A. C., Hall, B. A., Campbell, I. D. & Sansom, M. S. P. A Helix Heterodimer in a Lipid Bilayer: Prediction of the Structure of an Integrin Transmembrane Domain via Multiscale Simulations. *Structure (London, England : 1993)* **19,** 1477–1484 (2011).
40. Stansfeld, P. J., Jefferys, E. E. & Sansom, M. S. P. Multiscale simulations reveal conserved patterns of lipid interactions with aquaporins. *Structure (London, England : 1993)* **21,** 810–819 (2013).
41. Stansfeld, P. J., Hopkinson, R., Ashcroft, F. M. & Sansom, M. S. P. PIP(2)-binding site in Kir channels: definition by multiscale biomolecular simulations. *Biochemistry* **48,** 10926–10933 (2009).
42. Liu, R., Li, Y. & Liu, L. Single molecule fluorescence spectroscopy for quantitative biological applications. *Quant Biol* **4,** 177–191 (2016).
43. Stone, M. B., Shelby, S. A. & Veatch, S. L. Super-Resolution Microscopy: Shedding Light on the Cellular Plasma Membrane. *Chem. Rev.* **117,** 7457–7477 (2017).
44. Dunne, P. D. *et al.* DySCo: quantitating associations of membrane proteins using two-color single-molecule tracking. *Biophys. J.* **97,** L5–7 (2009).
45. Veya, L., Piguet, J. & Vogel, H. Single Molecule Imaging Deciphers the Relation between Mobility and Signaling of a Prototypical G Protein-coupled Receptor in Living Cells. *Journal of Biological Chemistry* **290,** 27723–27735 (2015).
46. Brandsma, A. M. *et al.* Mechanisms of inside-out signaling of the high-affinity IgG receptor FcγRI. *Sci Signal* **11,** (2018).
47. Zanetti-Domingues, L. C. *et al.* The architecture of EGFR's basal complexes reveals autoinhibition mechanisms in dimers and oligomers. *Nat Commun* **9,** 4325 (2018).
48. Low-Nam, S. T. *et al.* ErbB1 dimerization is promoted by domain co-confinement and stabilized by ligand binding. *Nat. Struct. Mol. Biol.* **18,** 1244–1249 (2011).
49. Steinkamp, M. P. *et al.* erbB3 Is an Active Tyrosine Kinase Capable of Homo- and Heterointeractions. *Molecular and Cellular Biology* **34,** 965–977 (2014).
50. Wang, Y., Bugge, K., Kragelund, B. B. & Lindorff-Larsen, K. Role of protein dynamics in transmembrane receptor signalling. *Curr. Opin. Struct. Biol.* **48,** 74–82 (2018).
51. Sharpe, H. J., Stevens, T. J. & Munro, S. A Comprehensive Comparison of Transmembrane Domains Reveals Organelle-Specific Properties. *Cell* **142,** 158–169 (2010).
52. Russ, W. P. & Engelman, D. M. The GxxxG motif: A framework for transmembrane helix-helix association. *J. Mol. Biol.* **296,** 911–919 (2000).
53. Teese, M. G. & Langosch, D. Role of GxxxG Motifs in Transmembrane Domain Interactions. *Biochemistry* **54,** 5125–5135 (2015).
54. Walters, R. F. S. & DeGrado, W. F. Helix-packing motifs in membrane proteins. *Proc. Natl. Acad. Sci. U.S.A.* **103,** 13658–13663 (2006).
55. Chothia, C., Levitt, M. & Richardson, D. Helix to helix packing in proteins. *J. Mol. Biol.* **145,** 215–250 (1981).
56. Polyansky, A. A., Volynsky, P. E. & Efremov, R. G. Multistate organization of transmembrane helical protein dimers governed by the host membrane. *J. Am. Chem. Soc.* **134,** 14390–14400 (2012).
57. Prakash, A., Janosi, L. & Doxastakis, M. GxxxG motifs, phenylalanine, and cholesterol guide the self-association of transmembrane domains of ErbB2 receptors. *Biophys. J.* **101,** 1949–1958 (2011).
58. Petrache, H. I., Grossfield, A., MacKenzie, K. R., Engelman, D. M. & Woolf, T. B. Modulation of

glycophorin A transmembrane helix interactions by lipid bilayers: molecular dynamics calculations. *J. Mol. Biol.* **302,** 727–746 (2000).

59. Dominguez, L., Foster, L., Straub, J. E. & Thirumalai, D. Impact of membrane lipid composition on the structure and stability of the transmembrane domain of amyloid precursor protein. *Proc Natl Acad Sci USA* **113,** E5281–7 (2016).
60. Hong, H. & Bowie, J. U. Dramatic Destabilization of Transmembrane Helix Interactions by Features of Natural Membrane Environments. *J. Am. Chem. Soc.* **133,** 11389–11398 (2011).
61. Defour, J.-P. *et al.* Tryptophan at the transmembrane–cytosolic junction modulates thrombopoietin receptor dimerization and activation. *Proc. Natl. Acad. Sci. U.S.A.* **110,** 2540–2545 (2013).
62. Dhara, M. *et al.* v-SNARE transmembrane domains function as catalysts for vesicle fusion. *Elife* **5,** (2016).
63. Munter, L. M. *et al.* GxxxG motifs within the amyloid precursor protein transmembrane sequence are critical for the etiology of Abeta42. *EMBO J.* **26,** 1702–1712 (2007).
64. Berger, B. W. *et al.* Consensus motif for integrin transmembrane helix association. *Proc Natl Acad Sci USA* **107,** 703–708 (2010).
65. Heukers, R. *et al.* Endocytosis of EGFR requires its kinase activity and N-terminal transmembrane dimerization motif. *J. Cell. Sci.* **126,** 4900–4912 (2013).
66. Huang, Y. *et al.* Molecular basis for multimerization in the activation of the epidermal growth factor receptor. *Elife* **5,** 18756 (2016).
67. Endres, N. F. *et al.* Conformational coupling across the plasma membrane in activation of the EGF receptor. *Cell* **152,** 543–556 (2013).
68. Bugge, K., Lindorff-Larsen, K. & Kragelund, B. B. Understanding single-pass transmembrane receptor signaling from a structural viewpoint-what are we missing? *FEBS J.* **283,** 4424–4451 (2016).
69. Lelimousin, M., Limongelli, V. & Sansom, M. S. P. Conformational Changes in the Epidermal Growth Factor Receptor: Role of the Transmembrane Domain Investigated by Coarse-Grained MetaDynamics Free Energy Calculations. *J. Am. Chem. Soc.* **138,** 10611–10622 (2016).
70. Domański, J., Sansom, M. S. P., Stansfeld, P. J. & Best, R. B. Atomistic mechanism of transmembrane helix association. *PLoS Comput Biol* **16,** e1007919– (2020).
71. Wheldon, L. M. *et al.* Critical Role of FLRT1 Phosphorylation in the Interdependent Regulation of FLRT1 Function and FGF Receptor Signalling. *PLoS ONE* **5,** e10264– (2010).
72. Haines, B. P., Wheldon, L. M., Summerbell, D., Heath, J. K. & Rigby, P. W. J. Regulated expression of FLRT genes implies a functional role in the regulation of FGF signalling during mouse development. *Dev. Biol.* **297,** 14–25 (2006).
73. Leyva-Díaz, E. *et al.* FLRT3 is a Robo1-interacting protein that determines Netrin-1 attraction in developing axons. *Curr. Biol.* **24,** 494–508 (2014).
74. Forbes, S. A. *et al.* COSMIC: mining complete cancer genomes in the Catalogue of Somatic Mutations in Cancer. *Nucleic Acids Res.* **39,** D945–D950 (2010).
75. Stone, M. B., Shelby, S. A., Núñez, M. F., Wisser, K. & Veatch, S. L. Protein sorting by lipid phase-like domains supports emergent signaling function in B lymphocyte plasma membranes. *Elife* **6,** 212 (2017).
76. Lorent, J. H. *et al.* Structural determinants and functional consequences of protein affinity for membrane rafts. *Nat Commun* **8,** 1–10 (2017).
77. Lorent, J. H. *et al.* Plasma membranes are asymmetric in lipid unsaturation, packing and protein shape. *Nat. Chem. Biol.* **16,** 644–652 (2020).
78. Honig, B. & Shapiro, L. Adhesion Protein Structure, Molecular Affinities, and Principles of Cell-Cell Recognition. *Cell* **181,** 520–535 (2020).
79. Brasch, J., Harrison, O. J., Honig, B. & Shapiro, L. Thinking outside the cell: how cadherins drive adhesion. *Trends Cell Biol.* **22,** 299–310 (2012).
80. Wu, Y. *et al.* Cooperativity between trans and cis interactions in cadherin-mediated junction formation. *Proc Natl Acad Sci USA* **107,** 17592–17597 (2010).
81. Yin, Y. *et al.* EphA receptor tyrosine kinases interact with co-expressed ephrin-A ligands in cis. *Neuroscience Research* **48,** 285–295 (2004).
82. Carvalho, R. F. *et al.* Silencing of EphA3 through a cis interaction with ephrinA5. *Nat. Neurosci.* **9,** 322–330 (2006).
83. Jones, D. T. Protein secondary structure prediction based on position-specific scoring matrices 1 1Edited by G. Von Heijne. *J. Mol. Biol.* **292,** 195–202 (1999).
84. Pasquier, C. & Hamodrakas, S. J. An hierarchical artificial neural network system for the classification of transmembrane proteins. *Protein Eng.* **12,** 631–634 (1999).
85. Tusnady, G. E. & Simon, I. The HMMTOP transmembrane topology prediction server. *Bioinformatics* **17,** 849–850 (2001).
86. Eswar, N. *et al.* Comparative Protein Structure Modeling Using Modeller. *Current Protocols in Bioinformatics* **15,** 5.6.1–5.6.30 (2006).
87. Hess, B., Kutzner, C., Van Der Spoel, D. & Lindahl, E. GROMACS 4: Algorithms for Highly Efficient, Load-Balanced, and Scalable Molecular Simulation. *J. Chem. Theory Comput.* **4,** 435–447 (2008).

88. Pronk, S. *et al.* GROMACS 4.5: a high-throughput and highly parallel open source molecular simulation toolkit. *Bioinformatics* **29,** 845–854 (2013).
89. Monticelli, L. *et al.* The MARTINI Coarse-Grained Force Field: Extension to Proteins. *J. Chem. Theory Comput.* **4,** 819–834 (2008).
90. Marrink, S. J., de Vries, A. H. & Mark, A. E. Coarse Grained Model for Semiquantitative Lipid Simulations. *J Phys Chem B* **108,** 750–760 (2004).
91. Berendsen, H., Postma, J., Vangunsteren, W. F., DiNola, A. & Haak, J. R. Molecular-Dynamics with Coupling to an External Bath. *J. Chem. Phys.* **81,** 3684–3690 (1984).
92. Lee, J. *et al.* CHARMM-GUI Input Generator for NAMD, GROMACS, AMBER, OpenMM, and CHARMM/OpenMM Simulations Using the CHARMM36 Additive Force Field. *J. Chem. Theory Comput.* **12,** 405–413 (2016).
93. Lee, S. *et al.* CHARMM36 United Atom Chain Model for Lipids and Surfactants. *J Phys Chem B* **118,** 547–556 (2014).
94. Huang, J. & MacKerell, A. D. CHARMM36 all-atom additive protein force field: Validation based on comparison to NMR data. *J Comput Chem* **34,** 2135–2145 (2013).
95. Essmann, U. *et al.* A smooth particle mesh Ewald method. *J. Chem. Phys.* **103,** 8577–8593 (1995).
96. Hess, B. P-LINCS: A Parallel Linear Constraint Solver for Molecular Simulation. *J. Chem. Theory Comput.* **4,** 116–122 (2008).
97. Humphrey, W., Dalke, A. & Schulten, K. VMD: visual molecular dynamics. *J Mol Graph* **14,** 33–8, 27–8 (1996).
98. Aricescu, A. R., Lu, W. & Jones, E. Y. A time- and cost-efficient system for high-level protein production in mammalian cells. *Acta Crystallogr. D Biol. Crystallogr.* **62,** 1243–1250 (2006).
99. Webb, S. E. D., Needham, S. R., Roberts, S. K. & Martin-Fernandez, M. L. Multidimensional single-molecule imaging in live cells using total-internal-reflection fluorescence microscopy. *Opt Lett* **31,** 2157–2159 (2006).
100. Rolfe, D. J. *et al.* Automated multidimensional single molecule fluorescence microscopy feature detection and tracking. *Eur Biophys J* **40,** 1167–1186 (2011).